

## Research Article

# A Triple-Band Broadband Miniature Antenna Design for Implantable Continuous Glucose Monitoring

Zhiwei Song <sup>1</sup>, Xiaoming Xu <sup>1</sup>, Hongxiang Miao <sup>1</sup> and Lu Wang <sup>2</sup>

<sup>1</sup>School of Electrical Engineering, Xinjiang University, Huarui Street 777#, Shuimogou District, Wulumuqi, Xinjiang, China

<sup>2</sup>58th Research Institute of China Electronics Technology Group Corporation, Wuxi, China

Correspondence should be addressed to Zhiwei Song; [suzawer@163.com](mailto:suzawer@163.com)

Received 15 June 2023; Revised 20 September 2023; Accepted 27 September 2023; Published 13 October 2023

Academic Editor: Shobhit K. Patel

Copyright © 2023 Zhiwei Song et al. This is an open access article distributed under the Creative Commons Attribution License, which permits unrestricted use, distribution, and reproduction in any medium, provided the original work is properly cited.

This paper presents a miniaturized triband implantable planar antenna that covers the industrial, scientific, and medical (ISM) band and the Wireless Medical Telemetry Service (WMTS) band which can be used in a continuous blood glucose monitoring device. The antenna consists of a slotted radiating patch and a ground plane with a cross slot to miniaturize its size. The overall antenna size is only  $51.35 \text{ mm}^3$  ( $7.6 \times 7.6 \times 0.889 \text{ mm}^3$ ) due to the reduced size by the slotting technique. Compared to other implantable antennas with similar performance, the proposed antenna is smaller in size, simple in construction, and easy to be fabricated. By cutting a cross slot in GND, impedance matching is improved, especially at the two higher frequency bands. We have fabricated the prototype and carried out measurements. The results show its gains are  $-32.2 \text{ dBi}$ ,  $-18.8 \text{ dBi}$ , and  $-19.1 \text{ dBi}$  at 0.9 GHz, 1.4 GHz, and 2.45 GHz, respectively. Its radiation patterns have good symmetry in the two lower operating frequency bands. In addition, the maximum SAR values comply with the IEEE standard safety guidelines (IEEE C95.1-2019).

## 1. Introduction

With the demand for new telemedicine solutions, the research on implantable antennas that can be applied in biomedicine has become one of the most concerned and rapidly developing technologies. To provide remote medical services for patients, reliable wireless medical equipment and stable wireless networks must be the basic guarantee, such as wireless body area networks (WBANs) and implantable antennas [1, 2]. Using biomedical implantable antennas can help doctors diagnose and treat patients' lesions, continuously monitor medical conditions, and support new medical services for telemedicine [3–6]. Monitoring blood glucose is moving from finger-prick blood glucose measurement to implantable continuous monitoring, as traditional finger-prick blood glucose measurement methods are not continuous enough and cause painful sensations to patients [7–9].

To ensure patient comfort, miniaturized implantable antennas are an inevitable trend of development. As it is well known, the larger the relative dielectric constant of

a dielectric substrate, the shorter the wavelength corresponding to a certain resonant frequency, and half wavelength antennas have high radiation efficiency. Therefore, two general methods are currently used to decrease the dimensions of antennas: extended current paths and the use of high dielectric constant substrates [10–16]. In [10], Rogers 3010 ( $\epsilon_r = 10.2$ ) is used, and the authors cut two rectangular slots in the ring patch for longer current paths to achieve miniaturization, with a final dimension of  $120.69 \text{ mm}^3$ . In [11], the size of the antenna can be effectively reduced at a fixed frequency by embedding curved slots and six open slots in the ground and using two layers of Rogers 3010 ( $\epsilon_r = 10.2$ ) as a substrate. In [13], a meandering slot and eight open-ended rectangular slots are engraved on the radiation patch to minimize the size and expand the impedance bandwidth of the antenna, and the size of the antenna is  $99.69 \text{ mm}^3$ . In [14], the authors have minimized the antenna by extending the current path through a simple slotting method, and the final size of the antenna is  $88.09 \text{ mm}^3$ . In [15, 16], the miniaturized antenna is gained by slotting both the radiation patch and the ground plane.

In addition, improving the service life of implantable medical devices is also a research hotspot. Using the low power consumption of the aerial in the high-frequency band to wake up the device and the high power consumption in the low-frequency band to transmit data can prolong the life of the implanted medical device [17–21]. In [18], two short-circuit probes are introduced on the orthogonal band, enabling the antenna to operate in the WMTS band (1.4 GHz); the path connecting two asymmetric opening tails enables the antenna to work in the ISM band (2.45 GHz), and the dimension is  $103.7 \text{ mm}^3$ . In [19], a compact tri-band antenna consisting of a spiral radiation patch with an end opening slot on the ground plane, operating simultaneously in the MICS band (402 MHz), the WMTS band (1.4 GHz), and the ISM band (2.4 GHz), is proposed, with a dimension of  $197 \text{ mm}^3$ . In [20], the authors describe the design of a dual-band circular implantable antenna for biomedical applications. The antenna is proposed to work in both the MICS band and the ISM band, and its size is  $\pi \times 10^2 \times 2.54 \text{ mm}^3$ . In [21], three-band antenna embedding in lossy tissues with circular polarization (CP) behavior was proposed for biotelemetry applications, working in the ISM band (868 MHz and 2.4 GHz) and medium frequency band (1.824–1.98 GHz), and its size is  $10 \times 10 \times 1.016 \text{ mm}^3$ .

In summary, a miniaturized antenna with multi-operating frequency bands is an inevitable trend.

This paper presents a new tri-band implantable planar antenna with more compact dimensions ( $51.35 \text{ mm}^3$ ) and simple geometry for continuous blood glucose monitoring that can be implanted subcutaneously. Its bandwidths are 100 MHz (0.85–0.95 GHz, 11.1%), 150 MHz (1.31–1.46 GHz, 10.8%), and 680 MHz (2.19–2.87 GHz, 27.8%), so its working frequency band covers the ISM (0.9 GHz and 2.45 GHz) and WMST (1.4 GHz) frequency bands very well. The trifrequency bands and miniaturization of size are gained by cut slots in the radiation patch. Impedance matching is improved by cutting a cross slot in GND, especially in the two higher frequency bands. To further increase the bandwidth, the thickness of the dielectric substrate is properly adjusted. Finally, a model of the designed antenna is fabricated and tested. It is implanted into the biogel and pork powder for measurement, and the implantation depth is 4 mm. The results of the study demonstrate that the antenna has a simple geometry and excellent radiation characteristics.

## 2. Topology and Design Strategy

**2.1. Antenna Geometry and Simulation Environment.** The dimensions and geometry of the designed antenna are presented in Figure 1. The patch is displayed in Figure 1(a), and GND is displayed in Figure 1(b). Figure 1(c) shows a profile view of the designed antenna. The antenna consists of a superstrate, a radiation patch with multiple E-shaped and I-shaped slots, a substrate, a ground plane with a cross slot, and a coaxial probe. The radiation patch and GND are located on the top and bottom faces of the substrate, respectively. The meandering structure in the radiation patch is used to achieve miniaturization and multifrequency of the

antenna, and the cross slot in GND is to gain better impedance matching. The antenna is excited by a  $50 \Omega$  coaxial feed with a radius of 0.2 mm. By adjusting the feeding position ( $S = 0.45 \text{ mm}$ ,  $T = 0.4 \text{ mm}$ ), better impedance matching and trifrequency bands are achieved. The size of the antenna is  $51.35 \text{ mm}^3$ , and the superstrate can protect the radiation surface from contact with human tissue. The exact dimensions of the parameters of the antenna are listed in Table 1. To reduce the dimensions of the antenna, a high dielectric constant material ( $\epsilon_r = 10.2$ ) and slotting techniques are used, and its size is smaller than that of antennas reported in the literature. We optimize the radiation characteristics of the proposed antenna by using slotting techniques in the patch and GND.

All simulation analyses are performed when the antenna is implanted in a three-layer human tissue model, as shown in Figure 1(d). The three-layer human tissue model consists of a skin box with dimensions of  $80 \times 80 \times 4 \text{ mm}^3$ , a fat box with dimensions of  $80 \times 80 \times 4 \text{ mm}^3$ , and a muscle box with dimensions of  $80 \times 80 \times 30 \text{ mm}^3$ , and the simulated surroundings have the same dielectric constant as human tissues as shown in Table 2. For example, the conductivity at 0.9 GHz is 0.87 s/m, and the dielectric constant is 41.3 [22]. The antenna is implanted in the center of the cross section of the skin layer with a depth of 4 mm. High-frequency structure simulator 21.0 (HFSS) software is used to analyze how the key parameters affect antenna performance. These parameters are adjusted to extend the bandwidth and improve the impedance-matching characteristics.

**2.2. Evolution of Antenna Geometry.** The designed antenna achieves the design requirements in four steps. First, the original dimensions of the antenna are calculated by the following formula [21]:

$$f_r = \frac{c}{\lambda_g \sqrt{\epsilon_{\text{eff}}}} \approx \frac{c}{L_g \sqrt{\epsilon_r + 1/2}}, \quad (1)$$

where  $f_r$  is the resonant frequency,  $\lambda_g$  represents the guided wavelength,  $\epsilon_{\text{eff}}$  denotes the effective permittivity,  $\epsilon_r$  is the relative permittivity, and  $L_g$  is the antenna length, and the resonant frequency of the square patch antenna is calculated to be 5.5 GHz. As shown in Table 3 in the simulation, the triple frequency antenna is obtained by modifying the basic rectangular patch antenna design. In the absence of slots, the current distribution on the surface of the antenna conductor is generally uniform. Cutting E-shaped and F-shaped slots on the patch and a cross slot on the ground plane will cause the current to concentrate around the slot and interrupt the original current path on the conductor, requiring the current to bypass around the slot. Therefore, the current path is extended to achieve miniaturization. Simulation  $S_{11}$  of the above four cases is shown in Figure 2.

Case 1: open an E-shaped and F-shaped combination slot on the left side of the rectangular radiation patch

Case 2: cut two open-rectangular slots and one closed-rectangular groove on the right side of the rectangular radiation patch

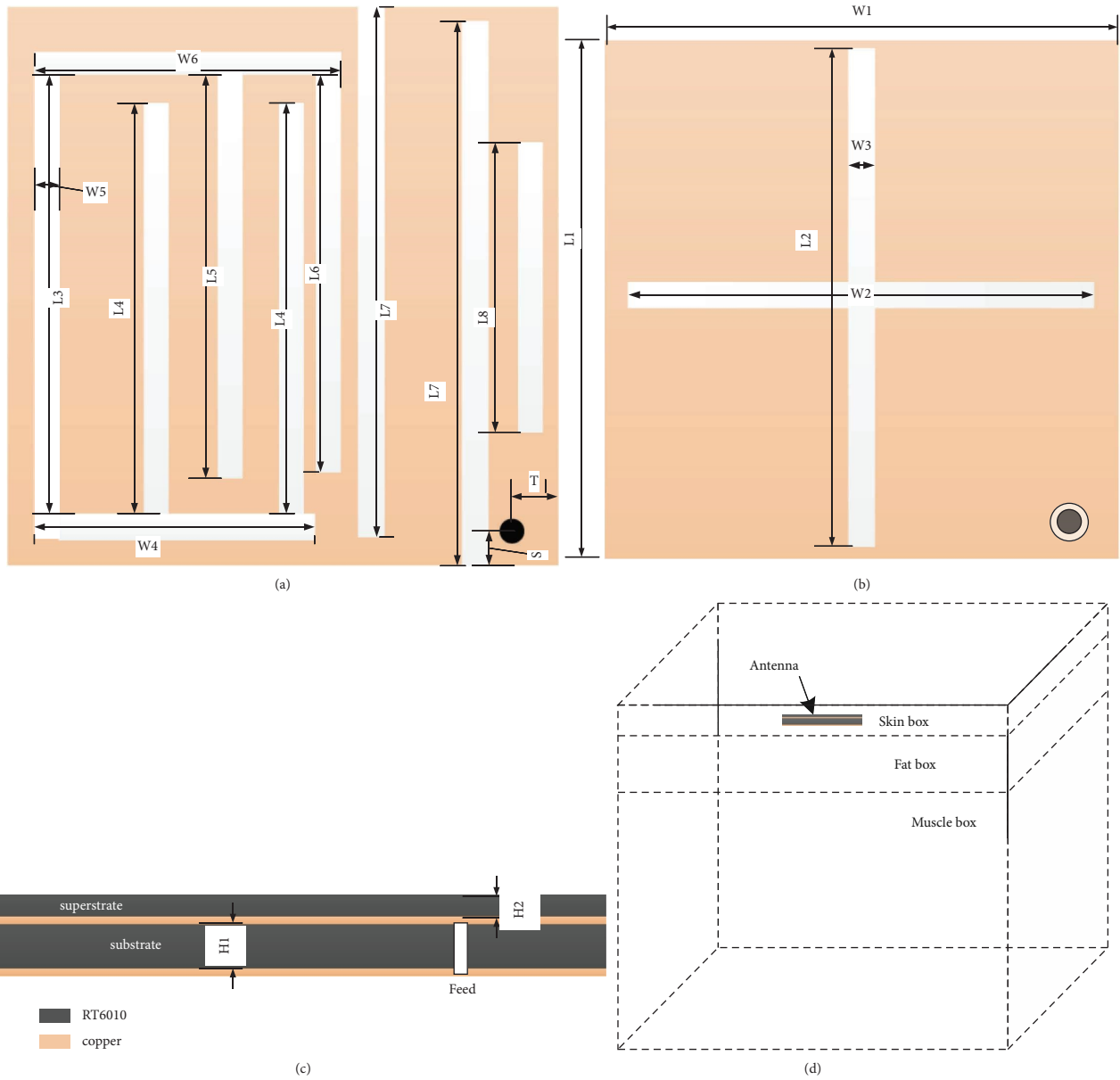


FIGURE 1: Designed triple-band antenna (not in scale). (a) Radiation patch with slots. (b) Ground plane with a cross slot. (c) Side-section view, the symmetrical coaxial feed port. (d) Antenna embedded in a single-skin model.

TABLE 1: Geometric parameters optimized for the proposed antenna (unit: mm).

Parameters	Value	Parameters	Value	Parameters	Value
$W_1$	7.6	$W_2$	6.6	$W_3$	0.6
$W_4$	4.15	$W_5$	0.4	$W_6$	4.65
$W_7$	4.65	$H_1$	0.635	$H_2$	0.254
$L_1$	7.6	$L_2$	7.4	$L_3$	6.4
$L_4$	6.1	$L_5$	6.2	$L_6$	6
$L_7$	7.4	$L_8$	5		

TABLE 2: Dielectric constant of human tissue.


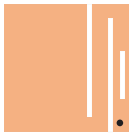






Tissue/frequency	0.9 GHz		1.4 GHz		2.45 GHz	
	$\epsilon_r$	$\sigma$ (s/m)	$\epsilon_r$	$\sigma$ (s/m)	$\epsilon_r$	$\sigma$ (s/m)
Skin	41.3	0.87	39.66	1.036	38.0	1.464
Fat	5.46	0.051	5.567	0.041	5.28	0.104
Muscle	55.0	0.948	54.112	1.1416	52.729	1.739

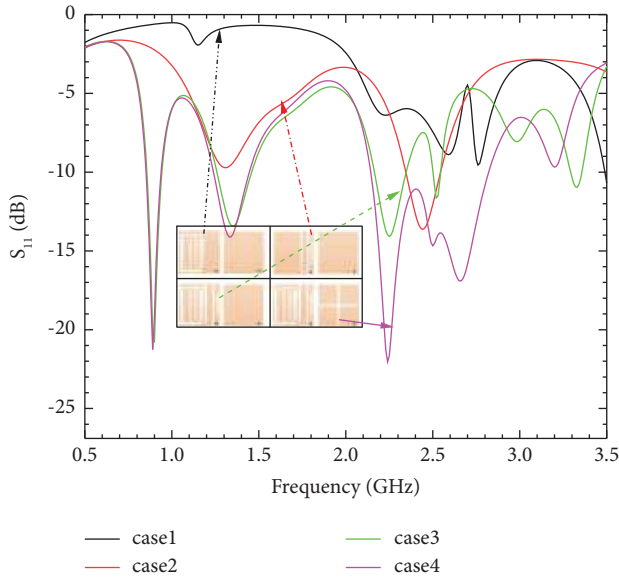
Case 3: open all the slots mentioned in step 1 and step 2 in the rectangular radiation patch

Case 4: the proposed antenna geometry adds a cross slot in GND

Simulated  $S_{11}$  of each case is shown in Figure 2. The black line in Figure 2 is simulated  $S_{11}$  of case 1. The central frequency of the fundamental mode of the antenna is 1.05 GHz. The size of the antenna has been greatly minimized by cutting a combined slot composed of an E-shaped slot and an F-shaped slot. The central frequency of high-order mode is about 2.5 GHz. The antenna structure operates close to the

TABLE 3: Antenna structure transformation process.

	(1)	(2)	(3)	(4)
Top view				
Bottom view				

FIGURE 2:  $S_{11}$  simulation results of four cases as shown in Table 3.

design goal and covers the ISM band (0.9 and 2.45 GHz). However, impedance matching is poor. The red line in Figure 2 is simulated  $S_{11}$  of case 2. Two working frequency bands are gained by cutting two open-ending rectangular slots and a closed rectangular slot. The central frequency of the fundamental mode is 1.3 GHz, and the central frequency of the high-order mode is 2.4 GHz. The antenna structure works in a band close to the design goal and covers the WMST band (1.4 GHz) and the ISM band (2.45 GHz). However, impedance matching is poor at 1.3 GHz. The green line in Figure 2 is simulated  $S_{11}$  of case 3, in which geometry is the combination of case 1 and case 2. The working frequency bands cover 0.9 GHz and 1.4 GHz, which meet our design goals, but the frequency band of 2.45 GHz is not good enough. In case 4, we have cut a cross slot on GND and changed the original current path, and the impedance matching in the highest frequency band is significantly improved, as shown by the purple line in Figure 2. In addition, the bandwidth of the 2.45 GHz band is well. From this, we can conclude that operating frequency bands of the antenna are shifted to the lower frequency band by cutting the E-shaped slot and F-shaped slot. The F-shaped slot is more effective than the E-shaped slot, and the cross slot on

the ground can better regulate the resonant frequency of the antenna.

**2.3. Key Parameter Simulation Analysis.** The dimensions of the proposed antenna are investigated, and this section describes what effect the key parameters have on the bandwidth and impedance matching of the antenna. A number of parameters are considered in the analysis of the proposed antenna, including the layer thickness of the dielectric substrate and superstrate, the length and width of the cross slot, and its position.

- (1) Simulated  $S_{11}$  of different sizes of substrate thickness ( $H_1$ ) and superstrate thickness  $H_2$  is shown in Figure 3(a). Due to the thickness of  $H_1$  and  $H_2$  being very small, the small change in their sizes can affect the electromagnetic field's distribution greatly, especially the magnetic field distribution. Therefore, the change in sizes of  $H_1$  and  $H_2$  affects both the bandwidth and impedance matching. When  $H_1 = 0.635$  mm and  $H_2 = 0.254$  mm, antenna performance is good in all three bands.
- (2) In case 4, we introduce a cross slot on the GND. As we know, the rectangular slot usually has a capacitance load in antenna design. Thus, the current density distribution and the current path of the antenna will change due to capacitive loading. The length and width of slots affect the size of capacitive loading. Antenna  $S_{11}$  simulated by two orthogonal rectangular slots of different dimensions ( $W_2$  and  $L_2$ ) is shown in Figure 3(b). As the simulated results show, the change in  $W_2$  and  $L_2$  affects the highest frequency band greatly, while the lower frequency bands remain unchanged. This may be due to the increase in gap capacitance, shifting the resonant band to higher frequencies, more information we can reference Figure 4. Antenna performance is good when  $W_2 = 3.3$  mm and  $L_2 = 3.7$  mm.
- (3) When the values of parameters  $W_5$  and  $L_8$  change, the simulated return loss is shown in Figure 3(c). In the low-frequency band, when  $W_5 = 0.2$  mm, the 0.9 GHz frequency band cannot be completely covered. In the high-frequency band, when

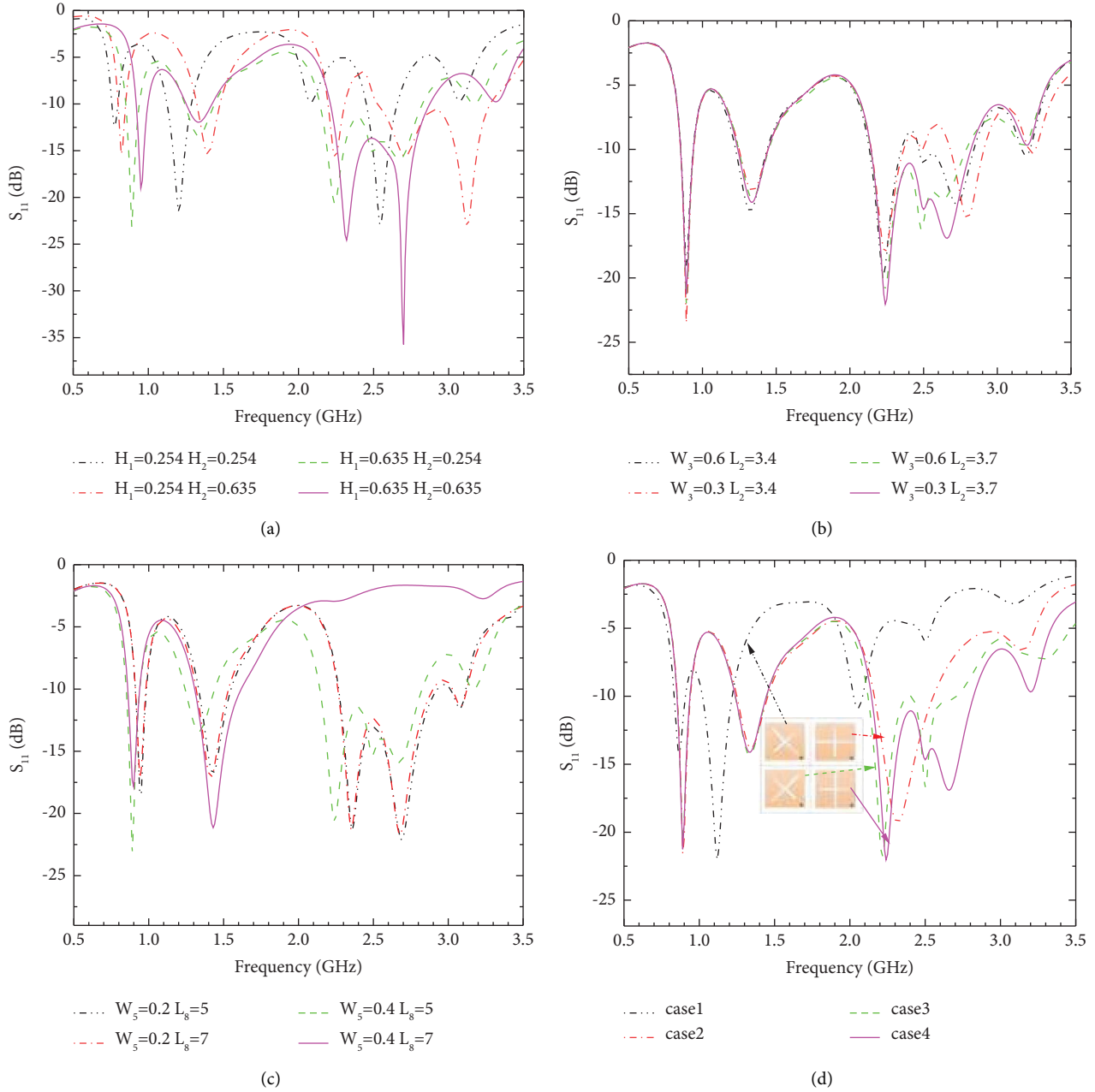


FIGURE 3: Effect of some parameters and cross-slot position on antenna performance. (a)  $H_1$  and  $H_2$ . (b)  $W_2$  and  $L_2$ . (c)  $W_5$  and  $L_8$ . (d) Rotation of the cross slot.

$L_8 = 7$  mm, the 2.45 GHz frequency band cannot be covered. Uniform incremental changes in the individual slot widths lead to uniform changes in the equivalent slot capacitance; thus, approximately the same offset is observed in all three frequency bands.

- (4) Simulated  $S_{11}$  when the cross slot is rotated is shown in Figure 3(d). When it is rotated by  $45^\circ$ , the antenna covers the 0.9 GHz band only. When it is with  $90^\circ$  rotation, the antenna covers the ISM and WMTS bands but has a narrow bandwidth at 2.45 GHz. When it is with  $135^\circ$  rotation, antenna covers the ISM and WMTS bands, but not very well.

### 3. Simulation Result Analysis

**3.1. Research on the Working Mechanism of the Antenna.** To understand the working principle of the antenna further, the simulated surface current distributions with different resonant frequencies at the same phase are shown in Figure 4. As shown in Figure 4(a), the current is mainly concentrated in the middle of the radiation patch at 0.9 GHz. At 1.4 GHz, currents are concentrated in the middle and right parts of the radiation patch. There are little currents distributed in GND, as shown in Figures 4(d) and 4(e). At 2.45 GHz, the current distribution is mainly in the right-hand part of the radiation patch, as shown in Figure 4(c). There is a lot of current

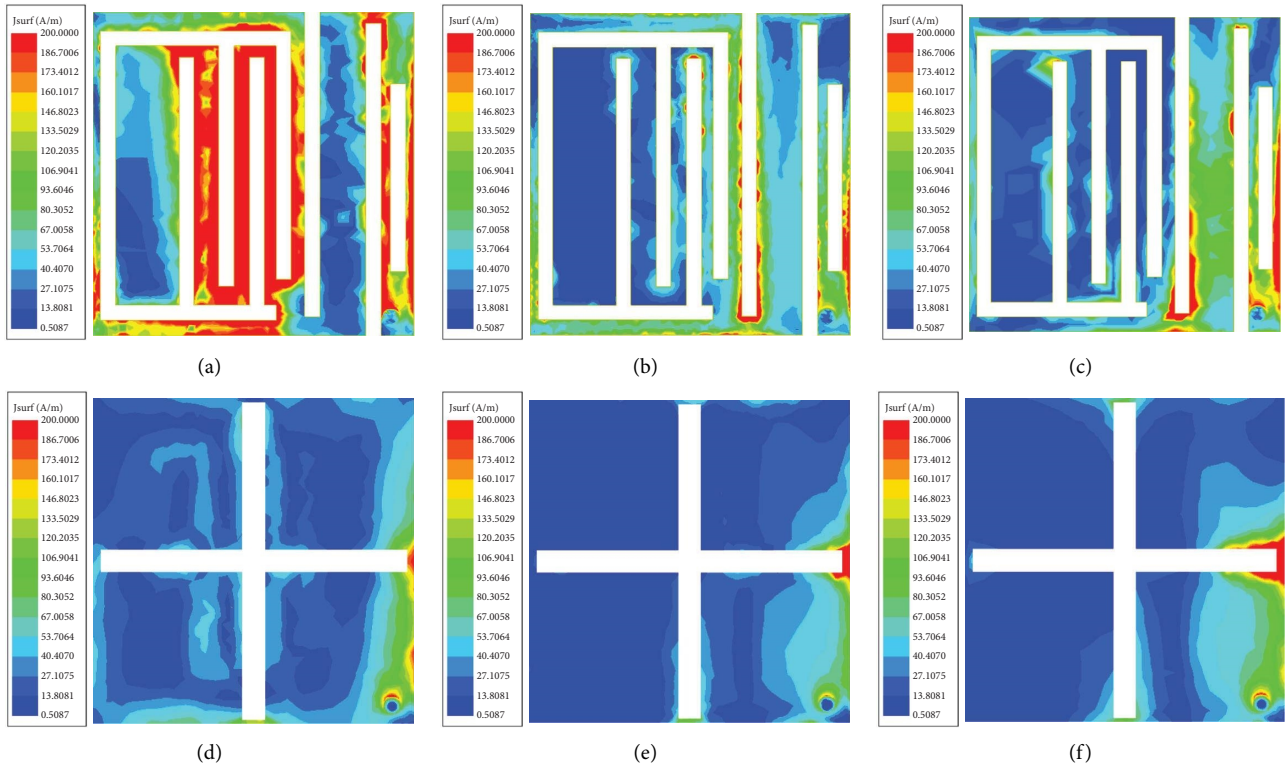


FIGURE 4: Current distribution on the radiation patch and GND. (a) 0.9 GHz patch; (d) 0.9 GHz GND; (b) 1.4 GHz patch; (e) 1.4 GHz GND; (c) 2.45 GHz patch; (f) 2.45 GHz GND.

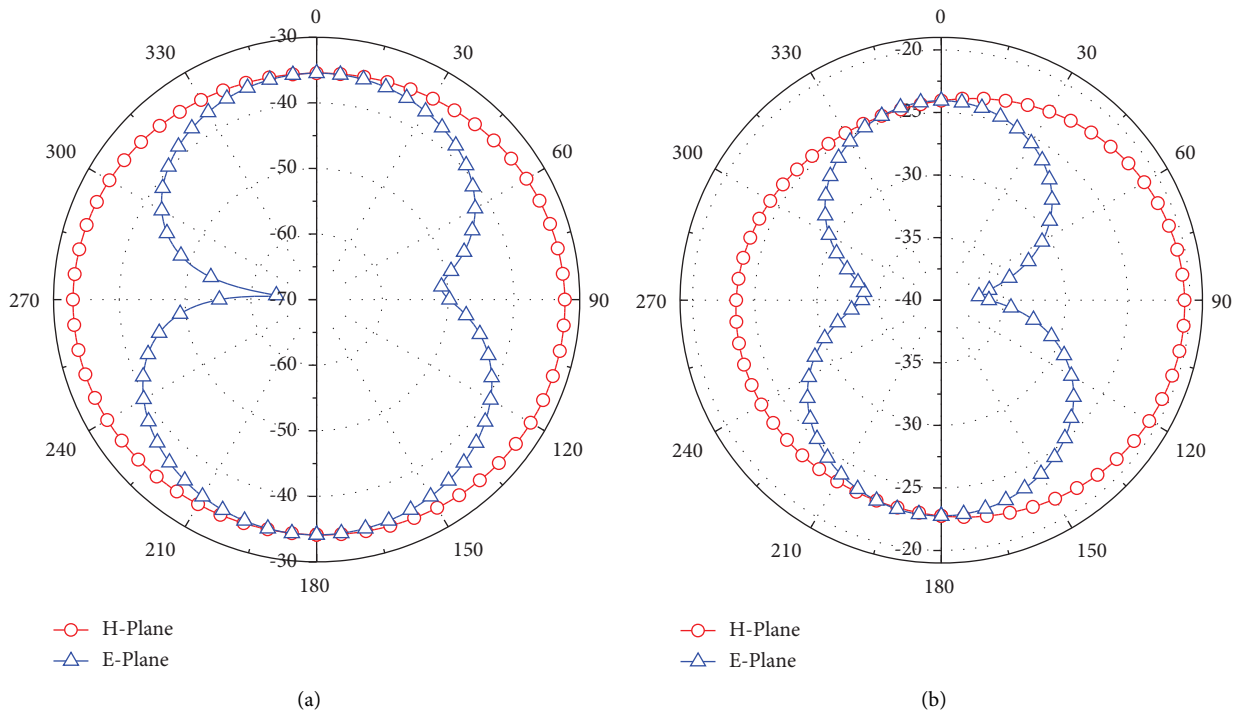


FIGURE 5: Continued.

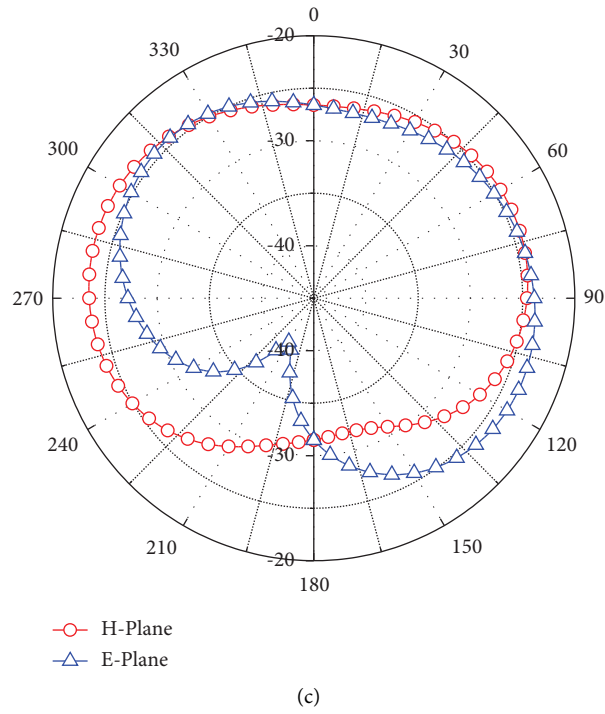


FIGURE 5: Simulated E-plane and H-plane radiation patterns. (a) 0.9 GHz; (b) 1.4 GHz; (c) 2.45 GHz.

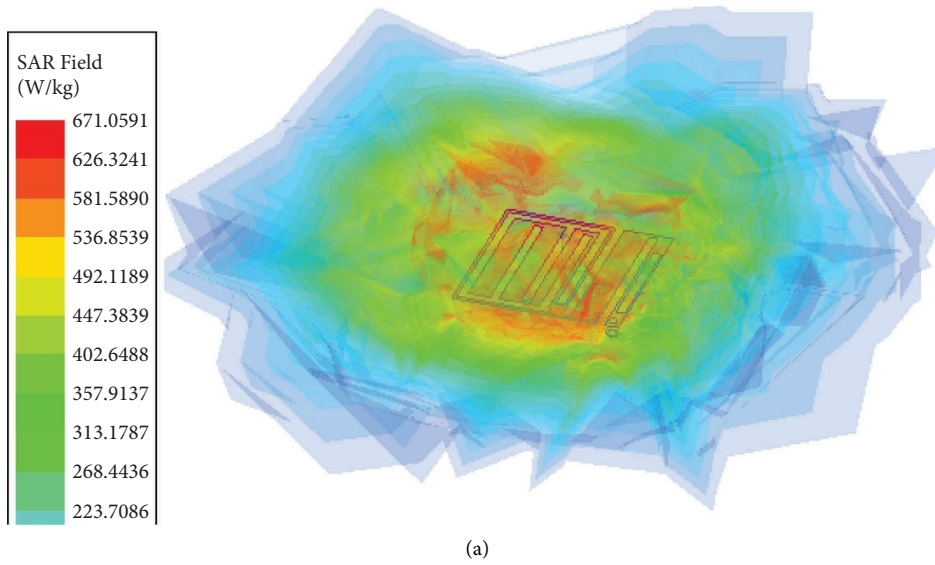


FIGURE 6: Continued.

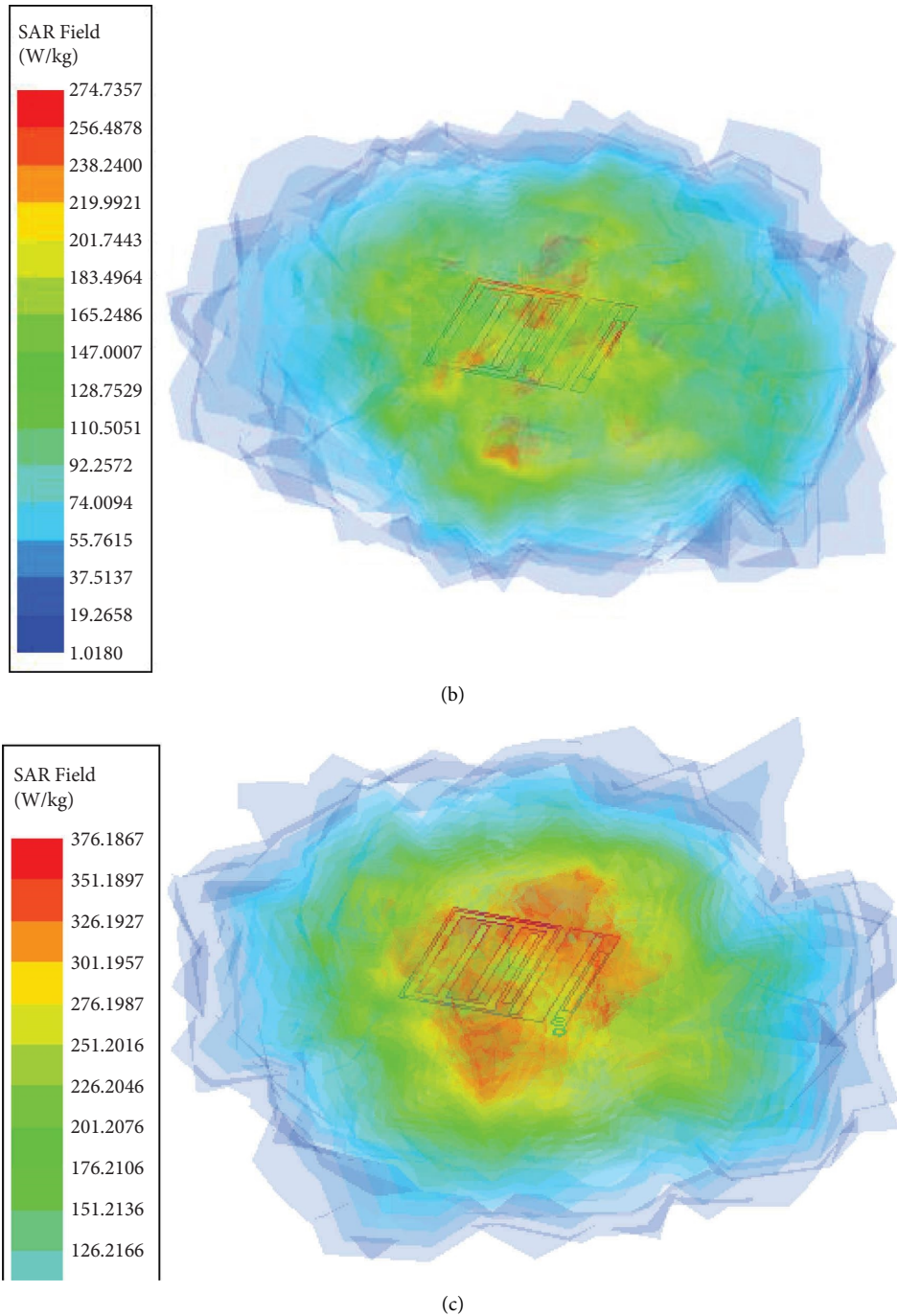


FIGURE 6: SAR distribution in the skin model (1g). (a) 0.9 GHz; (b) 1.4 GHz; (c) 2.45 GHz.

distribution in GND at 2.45 GHz, as displayed in Figure 4(f). Figure 4 more intuitively shows the structural principle of forming three operating frequency bands; that is, longer current paths correspond to lower operating frequencies. Furthermore, the impedance matching in the 2.45 GHz band is strongly influenced by the cross-slot loading owing to the large current intensity distribution in the ground plane. As shown in Figure 4(f), the current distribution around the horizontal slot is greater than that around the vertical slot.

Therefore, the effect of a change of the length of the horizontal slot ( $W_2$ ) on impedance matching is greater than the effect caused by the change of length ( $L_2$ ) of the vertical slot. This phenomenon further confirms our analysis of Figure 4 in the previous section.

The radiation principle of a PIFA antenna is similar to that of a microstrip antenna. That is, the operating frequency of a PIFA can be approximated by the empirical formula for the working frequency of a microstrip antenna [23]:



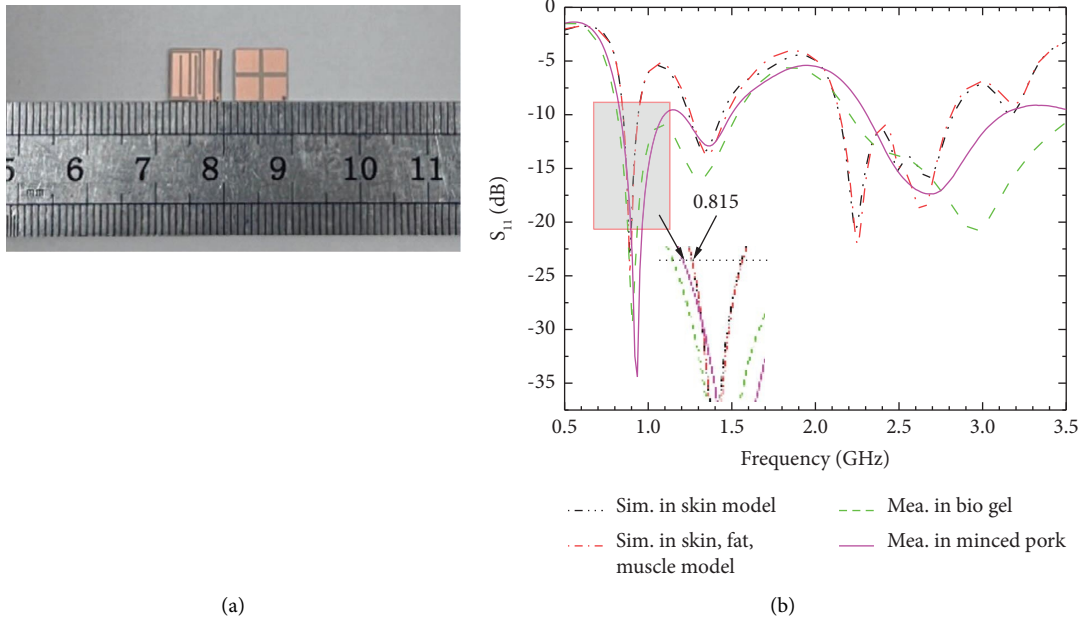


FIGURE 7: (a) Photo of the prototype and (b) comparison of simulated and measured  $S_{11}$ .

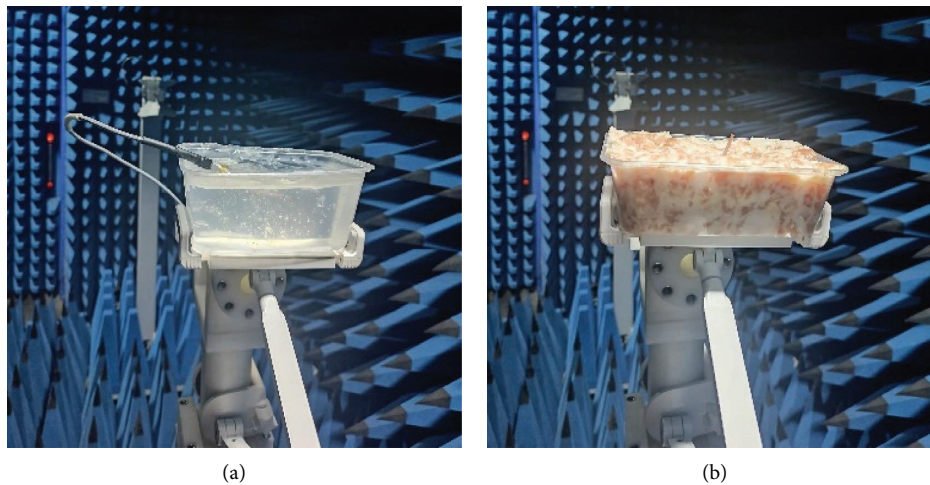


FIGURE 8: Antenna photos when tested in minced pork and biogel. (a) Biogel and (b) minced pork.

$$f_r = \frac{c}{4(w+l)\sqrt{\epsilon_r}}, \quad (2)$$

where  $f_r$  is the frequency of resonance,  $w$  denotes the width of the antenna,  $l$  represents the length of the antenna, and  $\epsilon_r$  is the relative permittivity. The resonant frequency of the antenna is calculated to be 0.88 GHz by combining the current distribution diagram and the formula.

**3.2. Far-Field Performance and SAR Evaluation.** The radiation patterns at 0.9 GHz, 1.4 GHz, and 2.45 GHz of the antenna have been simulated in a three-layer skin model of an adult man, as shown in Figure 5. At 0.9 GHz, 1.4 GHz, and 2.45 GHz, the far-field peak gains are  $-32.2$  dBi,  $-18.8$  dBi, and  $-19.2$  dBi, respectively.

At 0.9 GHz and 1.4 GHz, the antenna has approximately omnidirectional radiation patterns. When these two frequency bands are used for communication, the approximate omnidirectional radiation characteristics help alleviate the mismatch problem caused by changes in the direction of electromagnetic waves transmitted and received and improve the stability of wireless communication systems. In the 2.45 GHz band, the antenna features high gain and low power consumption. When this frequency band is used to wake up the implanted device, it can significantly reduce the power consumption of the implanted device, thereby extending its service life.

The specific absorption rate (SAR) is a very critical performance indicator for implantable antennas. If the implanted antenna radiates excessive power, it is easy to cause local overheating of human tissue, which will adversely

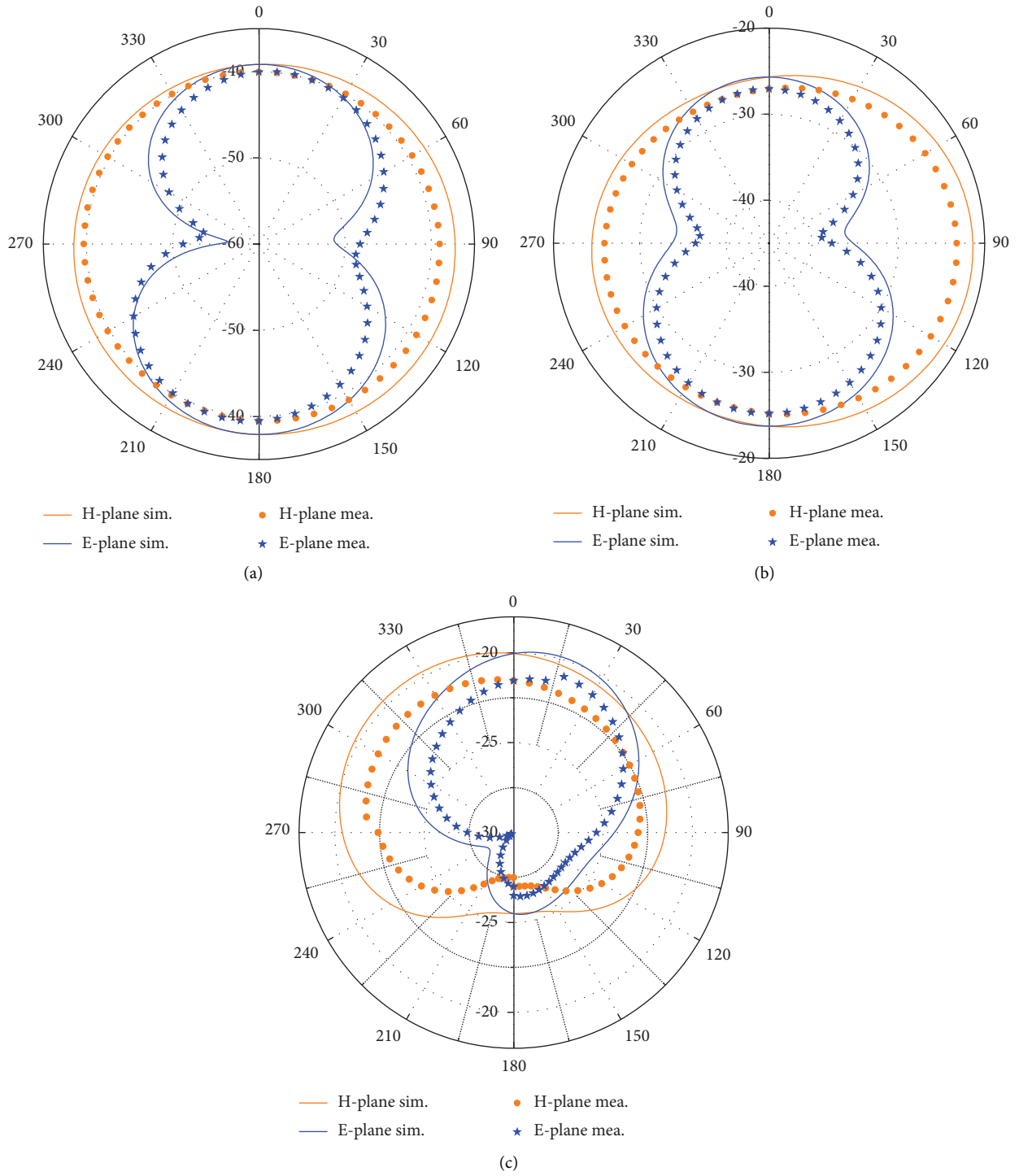


FIGURE 9: Comparisons of the measured and simulated radiation patterns. (a) 0.9 GHz, (b) 1.4 GHz, and (c) 2.45 GHz.

TABLE 4: comparison of the proposed antenna with recent works.

Ref.	Volume in $\lambda_0$ ( $\text{mm}^3$ )	Freq. (GHz)	Percent bandwidth (%)	Gain (dBi)	SAR (1-g)
[6]	$0.021 \times 0.021 \times 0.0006$	0.915	11.75	-27.65	730.1
		2.45	22.86	-22.99	591.4
[13]	$\pi \times 0.04^2 \times 0.0102$	2.45	21.22	-26.4	712.1
[15]	$0.024 \times 0.018 \times 0.0015$	0.915	9.83	-28.5	971
		2.45	8.57	-22.8	807
[18]	$\pi \times 0.024^2 \times 0.0059$	1.4	21.29	-32	702
		2.45	21.22	-31.6	781
[19]	$\pi \times 0.015^2 \times 0.0007$	0.4	23.25	-33.3	241
		1.4	14.43	-21.9	269
		2.45	18.12	-19.6	290
[21]	$0.029 \times 0.029 \times 0.0029$	0.86	15.58	-31.8	428
		1.85	7.46	-21.8	438
		2.45	18.69	-18.5	382
This work	$0.023 \times 0.023 \times 0.0027$	0.9	11.11	-32.2	671
		1.4	10.71	-18.8	275
		2.45	27.76	-19.1	376

TABLE 5: parameters of the link budget.

Transmitter			
Operating frequency (GHz)	0.9	1.4	2.45
Tx power $P_t$ (dBm)	2.92	7.12	5.21
Tx antenna gain $G_t$ (dBi)	-32.2	-18.8	-19.1
Receiver			
Rx antenna gain $G_r$ (dBi)	2.15	2.15	2.15
Ambient temperature $T_0$ (K)	CP	CP	CP
Receiver noise figure NF (dB)	293	293	293
Boltzmann constant $k$	$1.38 \times 10^{-23}$	$1.38 \times 10^{-23}$	$1.38 \times 10^{-23}$
Noise power density (dB/Hz)	-199.95	-199.95	-199.95
Propagation			
Bit rate $B_r$ (Mb/s)	1	1	1
Bit error rate	$1.0 \times 10^{-5}$	$1.0 \times 10^{-5}$	$1.0 \times 10^{-5}$
$E_b/N_0$ (ideal-BPSK) (dB)	9.6	9.6	9.6
Coding gain (dB)	0	0	0
Fixing deterioration $G_d$ (dB)	2.5	2.5	2.5

affect human health [24, 25]. The simulation results of SAR are shown in Figure 6. Since electromagnetic energy is deposited in human tissue, it is important to evaluate the safety of implanted recipients.

To maintain the SAR values in the specified range, the maximum 1 g average SAR values for 0.9 GHz, 1.4 GHz, and 2.4 GHz are 671 W/kg, 275 W/kg, and 376 W/kg, respectively, assuming an antenna transmitting frequency of 1 W. Therefore, the maximum transmission power should be less than 2.38 mW, 5.73 mW, and 4.19 mW to satisfy the FCC-established IEEE C95.1-2019 standard.

#### 4. Measurement Result Analysis

A prototype of the antenna is shown in Figure 7(a). An Agilent vector network analyzer (PNA-X) and a microwave darkroom developed by Electronics Forty-One are used for the physical measurements of the antenna. The actual test

environment is simulated using minced meat and biogel, as displayed in Figure 8. The biogel comprised deionized water (58.2%), Triton X-100 (36.7%), and diethylene glycol butyl ether (5.1%). Simulated and measured  $S_{11}$  are shown in Figure 7(b). The antenna measurement bandwidths are 240 MHz (0.85–1.09 GHz), 290 MHz (1.2–1.49 GHz), and 800 MHz (2.3–3.1 GHz) in skin gel tissue. In fresh ground pork tissue, the bandwidths are 0.69 GHz (0.83–1.52 GHz) and 1.29 GHz (2.21–3.5 GHz), respectively. In Figure 7(b), measured  $S_{11}$  are very well-matched with simulated  $S_{11}$  (simulation results in the single-layer skin model are represented by the black line, and simulation results in the skin, fat, and muscle model are represented by the red line) at 0.9 GHz. Nevertheless, there are small deviations between the simulated results and the two measurements at 1.4 GHz and 2.4 GHz. Reason  $f$  is that the test environment is very close but not identical to the simulated environment. The higher the frequency, the greater the difference in electrical

characteristics, making the deviation between the measurement results and the simulation results more significant.

The testing scenario for the remote radiation characteristics of the antenna is shown in Figure 9. The measured and simulated remote radiation patterns of the antenna at three operating frequency points have quasi-omnidirectional radiation characteristics.

To visually demonstrate the performance of the antennas designed in this paper, we list the main performance indicators of the antennas implanted in references and this work in Table 4. Compared with the literature antenna, the proposed antenna is further optimized in size, but the bandwidth and SAR value are still lacking. For example, SAR is better at 0.9 GHz in [21].

## 5. Link Budget

In order to gain a more comprehensive understanding of the data transmission capacity of the antenna, we have calculated its link margin (LM). Due to the fact that the human body is a multilayer lossy medium, the interior of the human body is a complex electromagnetic environment. So we simplified the external propagation link to a free-space model, with dB as the unit, and the formula of path loss  $L_f$  is as follows [26]:

$$L_f = 20 \log_{10} \left( \frac{4\pi d}{\lambda} \right), \quad (3)$$

where  $d$  is the distance between Tx and Rx antennas and  $\lambda$  represents the free space wavelength corresponding to the operating frequency point. The link margin (LM) is used to measure the communication performance of the implanted antenna. LM can be calculated as follows [26]:

$$\begin{aligned} LM &= \text{CNR}_{\text{link}} - \text{CNR}_{\text{required}}, \\ \text{CNR}_{\text{link}} &= P_t + G_t + G_r - L_f - N_0, \\ \text{CNR}_{\text{required}} &= \frac{E_b}{N_0} + 10 \log_{10} B_r - G_c + G_d, \\ N_0 &= 10 \log_{10} k + 10 \log_{10} T_i, \\ T_i &= T_0 (\text{NF} - 1). \end{aligned} \quad (4)$$

The parameters required in calculation are listed in Table 5.

We assume the ratio of the signal power is received by the external antenna at a certain distance and the noise power density when the implanted antenna is transmitted at a certain power [26]. CNR required refers to the carrier-to-noise ratio required by the receiving end to meet the requirements of a certain communication rate and bit error rate and is related to the sensitivity of the receiver. Here, we adopt the BPSK modulation method, the bit error rate is required to be less than  $1 \times 10^{-5}$ , and the bit rate ( $B_r$ ) is 1 Mb/s. Currently, the input power of the antenna working at 0.9 GHz, 1.4 GHz, and 2.4 GHz frequency is 2.92 dBm, 7.12 dBm, and 5.21 dBm, and the external receiving antenna

adopts a circularly polarized antenna with a gain of 2.15 dBi. The transceiver distance reaches 5.6 m, 13.1 m, and 9.6 m when the communication link margin reached more than 20 dB at 0.9 GHz, 1.4 GHz, and 2.4 GHz.

## 6. Conclusion

This study describes the design and evaluation of a small triband implantable antenna for medical monitoring systems. The antenna is designed to work at 0.9 GHz, 1.4 GHz, and 2.45 GHz, and these frequencies are typically used in the ISM band and the WMTS band. To prove the actual radiation characteristics of the antenna, a prototype is constructed and tested in biogel and minced pork. The measurements demonstrate that the  $-10$  dB bandwidth covers the required frequency band well, and its radiation patterns have good symmetry. In addition, the small size and good radiation characteristics of the antenna make it ideally suited for medical applications where implantable equipment is required.

## Data Availability

The relevant data are uploaded in the form of files.

## Conflicts of Interest

The authors declare that they have no conflicts of interest.

## Acknowledgments

This research was funded in part by the National Natural Science Foundation of China, under Grant 62261052; in part by the Xinjiang Uygur Autonomous Region Natural Science Foundation General Project, under Grant 2022D01C424; in part by the Tianchi Talent Project in Xinjiang Uygur Autonomous Region, under Grant 510523005137; the Xinjiang University, under Grant 620321063; and in part by the China Postdoctoral Science Foundation, under Grant 2022M722962.

## Supplementary Materials

The HFSS simulation data involved in Figure 2 are provided in a text document named Figure 2.txt. The HFSS simulation data involved in Figures 3(a–d) are provided as text documents named Figure 3(a).txt, Figure 3(b).txt, Figure 3(c).txt, and Figure 3(d).txt. The HFSS simulation data involved in Figures 5 (a–c) are provided in text documents named Figure 5(a).txt, Figure 5(b).txt, and Figure 5(c).txt. The HFSS simulation data involved in Figure 7(b) are provided in a text document named Figure 7(b).txt. The HFSS simulation data and measured data involved in Figure 9(a) are provided in a text document named Figure 9(a).txt. The HFSS simulation data and measured data involved in Figure 9(b) are provided in a text document named Figure 9(b).txt. The HFSS simulation data and measured data involved in Figure 9(c) are provided in a text document named Figure 9(c).txt. (*Supplementary Materials*)

## References

- [1] W. Liao, J. Shi, and J. Wang, "Electromagnetic interference of wireless power transfer system on wearable electrocardiogram," *IET Microwaves, Antennas & Propagation*, vol. 11, no. 3, pp. 330–335, 2017.
- [2] R. Cavallari, F. Martelli, R. Rosini, C. Buratti, and R. Verdone, "A survey on wireless body area networks: technologies and design challenges," *IEEE Communications Surveys & Tutorials*, vol. 16, no. 3, pp. 1635–1657, 2014.
- [3] A. F. Demir, Q. H. Abbasi, Z. E. Ankarali et al., "Anatomical region-specific in vivo wireless communication channel characterization," *IEEE Journal of Biomedical and Health Informatics*, vol. 21, no. 5, pp. 1254–1262, 2017.
- [4] K. S. Sultan and A. M. Abbosh, "Wearable dual polarized electromagnetic knee imaging system," *IEEE Transactions on Biomedical Circuits and Systems*, vol. 16, no. 2, pp. 296–311, 2022.
- [5] K. S. Sultan, B. Mohammed, P. C. Mills, and A. Abbosh, "Anthropomorphic durable realistic knee phantom for testing electromagnetic imaging systems," *IEEE Journal of Electromagnetics, RF and Microwaves in Medicine and Biology*, vol. 5, no. 2, pp. 132–138, 2021.
- [6] F. Faisal, M. Zada, A. Ejaz, Y. Amin, S. Ullah, and H. Yoo, "A miniaturized dual-band implantable antenna system for medical applications," *IEEE Transactions on Antennas and Propagation*, vol. 68, no. 2, pp. 1161–1165, 2020.
- [7] Z. Xiao, X. Tan, X. Chen et al., "An implantable RFID sensor tag toward continuous glucose monitoring," *IEEE Journal of Biomedical and Health Informatics*, vol. 19, no. 3, pp. 1–919, 2015.
- [8] X. Y. Liu, Z. T. Wu, Y. Fan, and E. M. Tentzeris, "A miniaturized CSRR loaded wide-beamwidth circularly polarized implantable antenna for subcutaneous real-time glucose monitoring," *IEEE Antennas and Wireless Propagation Letters*, vol. 16, pp. 577–580, 2017.
- [9] T. Yilmaz, R. Foster, and Y. Hao, "Broadband tissue mimicking phantoms and a patch resonator for evaluating non-invasive monitoring of blood glucose levels," *IEEE Transactions on Antennas and Propagation*, vol. 62, no. 6, pp. 3064–3075, 2014.
- [10] R. Li, Y.-X. Guo, B. Zhang, and G. Du, "A miniaturized circularly polarized implantable annular-ring antenna," *IEEE Antennas and Wireless Propagation Letters*, vol. 16, pp. 2566–2569, 2017.
- [11] C. Liu, Y.-X. Guo, and S. Xiao, "A hybrid patch/slot implantable antenna for biotelemetry devices," *IEEE Antennas and Wireless Propagation Letters*, vol. 11, pp. 1646–1649, 2012.
- [12] F. Faisal, M. Zada, H. Yoo, I. B. Mabrouk, M. Chaker, and T. Djerafi, "An ultra-miniaturized antenna with ultra-wide bandwidth for future cardiac leadless pacemaker," *IEEE Transactions on Antennas and Propagation*, vol. 70, no. 7, pp. 5923–5928, 2022.
- [13] W. Cui, R. Liu, L. Wang, M. Wang, H. Zheng, and E. Li, "Design of wideband implantable antenna for wireless capsule endoscope system," *IEEE Antennas and Wireless Propagation Letters*, vol. 18, no. 12, pp. 2706–2710, 2019.
- [14] Y. Zhang, C. Liu, X. Liu, K. Zhang, and X. Yang, "A wideband circularly polarized implantable antenna for 915 MHz ISM-band biotelemetry devices," *IEEE Antennas and Wireless Propagation Letters*, vol. 17, no. 8, pp. 1473–1477, 2018.
- [15] S. A. A. Shah and H. Yoo, "Scalp-implantable antenna systems for intracranial pressure monitoring," *IEEE Transactions on Antennas and Propagation*, vol. 66, no. 4, pp. 2170–2173, 2018.
- [16] C. Liu, Y.-X. Guo, R. Jegadeesan, and S. Xiao, "In vivo testing of circularly polarized implantable antennas in rats," *IEEE Antennas and Wireless Propagation Letters*, vol. 14, pp. 783–786, 2015.
- [17] L.-J. Xu, Y.-X. Guo, and W. Wu, "Dual-band implantable antenna with open-end slots on ground," *IEEE Antennas and Wireless Propagation Letters*, vol. 11, pp. 1564–1567, 2012.
- [18] L.-J. Xu, Z.-J. Chu, L. Zhu, J.-P. Xu, and Z. Duan, "Design and analysis of dual-band implantable antennas based on effective relative permittivity calculation," *IEEE Transactions on Antennas and Propagation*, vol. 69, no. 5, pp. 2463–2472, 2021.
- [19] T.-A. Le Trong, S. I. H. Shah, G. Shin, S. M. Radha, and I.-J. Yoon, "A compact triple-band antenna with a broadside radiation characteristic for head-implantable wireless communications," *IEEE Antennas and Wireless Propagation Letters*, vol. 20, no. 6, pp. 958–962, 2021.
- [20] N. Ganeshwaran, J. Jeyaprakash, M. Alsath, and V. Sathyanarayanan, "Design of a dual-band circular implantable antenna for biomedical applications," *IEEE Antennas and Wireless Propagation Letters*, vol. 19, no. 1, pp. 119–123, 2020.
- [21] Y. A. Kamel, H. A. Mohamed, H. Elsadek, and H. M. Elhennawy, "Miniaturized triple-band circular-polarized implantable patch antenna for bio-telemetry applications," *IEEE Antennas and Wireless Propagation Letters*, vol. 22, no. 1, pp. 74–78, 2023.
- [22] C. Gabriel, S. Gabriel, and E. Corthout, "The dielectric properties of biological tissues: I. Literature survey," *Physics in Medicine and Biology*, vol. 41, no. 11, pp. 2231–2249, 1996.
- [23] L. Dang, Z. Y. Lei, Y. J. Xie, G. L. Ning, and J. Fan, "A compact microstrip slot triple-band antenna for WLAN/WiMAX applications," *IEEE Antennas and Wireless Propagation Letters*, vol. 9, pp. 1178–1181, 2010.
- [24] IEEE, "IEEE standard for safety levels with respect to human exposure to electric, magnetic, and electromagnetic fields, 0 Hz to 300 GHz," in *IEEE Std C95.1-2019 (Revision of IEEE Std C95.1-2005/Incorporates IEEE Std C95.1-2019/Cor 1-2019)*, pp. 1–312, IEEE, Piscataway, NJ, USA, 2019.
- [25] K. Shahverdi, S. Hashemi, S. Sarafan, and H. Cao, "Triple-band implantable antenna design for biotelemetry applications in MICS/ISM/Wi-Fi/Bluetooth bands," *Technologies*, vol. 10, no. 4, p. 91, 2022.
- [26] K. Liu, R. Liu, W. Cui et al., "Design of conformal spiral dual-band antenna for wireless capsule system," *IEEE Access*, vol. 9, pp. 117349–117357, 2021.